nature biotechnology

Image-based analysis of lipid nanoparticle–mediated siRNA delivery, intracellular trafficking and endosomal escape

Jerome Gilleron[1], William Querbes[2], Anja Zeigerer[1], Anna Borodovsky[2], Giovanni Marsico[1], Undine Schubert[1], Kevin Manygoats[1], Sarah Seifert[1], Cordula Andree[1], Martin Stöter[1], Hila Epstein-Barash[2], Ligang Zhang[2], Victor Koteliansky[2], Kevin Fitzgerald[2], Eugenio Fava[1,3], Marc Bickle[1], Yannis Kalaidzidis[1,4], Akin Akinc[2], Martin Maier[2] & Marino Zerial[1]

Delivery of short interfering RNAs (siRNAs) remains a key challenge in the development of RNA interference (RNAi) therapeutics. A better understanding of the mechanisms of siRNA cellular uptake, intracellular transport and endosomal release could critically contribute to the improvement of delivery methods. Here we monitored the uptake of lipid nanoparticles (LNPs) loaded with traceable siRNAs in different cell types *in vitro* and in mouse liver by quantitative fluorescence imaging and electron microscopy. We found that LNPs enter cells by both constitutive and inducible pathways in a cell type-specific manner using clathrin-mediated endocytosis as well as macropinocytosis. By directly detecting colloidal-gold particles conjugated to siRNAs, we estimated that escape of siRNAs from endosomes into the cytosol occurs at low efficiency (1–2%) and only during a limited window of time when the LNPs reside in a specific compartment sharing early and late endosomal characteristics. Our results provide insights into LNP-mediated siRNA delivery that can guide development of the next generation of delivery systems for RNAi therapeutics.

In recent years, synthetic siRNAs have emerged as a promising therapeutic modality to silence disease-associated genes. Progress in creating efficient *in vivo* delivery systems has been critical for the development of numerous siRNA-based drugs currently undergoing human clinical trials[1]. *In vivo* intravenous delivery of siRNAs in an active form is a complex, multistep process. siRNAs have to (i) reach their target tissue and cells while avoiding RNase-mediated degradation and renal excretion; (ii) enter target cells, typically by endocytosis; (iii) cross the endosomal membrane to be released into the cytosol; (iv) bind to and get loaded onto the RNA-induced silencing complex (RISC) for silencing of the target gene[2]. Different systems have been developed for siRNA delivery by taking advantage of viruses[3] or of nonviral vectors such as liposomes, polycationic polymers, conjugates and nanoparticles. These approaches have various levels of efficiency and toxicity[4,5], but for most clinical indications they remain unsatisfactory.

LNPs are one of the most advanced delivery systems for siRNAs[6,7]. They comprise multiple lipids that self-assemble into 60- to 80-nm particles, thereby encapsulating the siRNA molecules. Efficient gene silencing in the liver has been demonstrated in multiple species, including nonhuman primates[8–10], even allowing for simultaneous silencing of multiple genes[9,11]. More recently, LNPs have shown robust mRNA silencing in human clinical trials[12,13]. Nevertheless, the precise molecular mechanisms underlying LNP-mediated delivery of siRNAs are not yet fully understood. We have previously demonstrated that the uptake of ionizable LNPs and gene silencing in the liver are dependent on Apolipoprotein E (ApoE) and low-density lipoprotein receptor (LDLR)-mediated endocytosis[14]. These results raise several questions. Which endocytic mechanisms are responsible for LNP uptake? To which endocytic compartments are LNPs transported and with which kinetics? Once internalized, how efficiently can siRNAs escape from endosomes? Are there cell-specific differences and how well do *in vitro* findings correlate with *in vivo* observations? Answering these questions could provide essential clues for further improvements in LNP-based siRNA delivery.

Previous attempts to address these questions have provided limited information largely due to the lack of reliable methods to visualize and quantify the uptake of LNPs and the cytosolic release of siRNAs. For example, up to now evidence for 'endosomal escape' has come either from cells treated with high concentrations of siRNAs (above the therapeutic range)[15] or indirectly as lack of co-localization to the pH-sensitive dye Lysotracker[16–18].

Here we developed an analytical platform based on a combination of quantitative light and electron microscopy (EM) to dissect the mechanisms of LNP-mediated siRNA delivery with high resolution. Our methodological approach permits us to resolve and quantify siRNA uptake, trafficking and escape from endosomes in time and space, at therapeutically relevant concentrations, both *in vitro* and *in vivo*.

[1]Max Planck Institute of Molecular Cell Biology and Genetics, Dresden, Germany. [2]Alnylam Pharmaceuticals, Cambridge, Massachusetts, USA. [3]German Center for Neurodegenerative Diseases, Bonn, Germany. [4]Moscow State University, Faculty of Bioengineering and Bioinformatics, Moscow, Russia. Correspondence should be addressed to M.Z. (zerial@mpi-cbg.de).

Received 27 March; accepted 13 May; published online 23 June 2013; doi:10.1038/nbt.2612

RESULTS

Development of LNPs loaded with traceable siRNAs

To measure the uptake, intracellular distribution, release into the cytosol and silencing activity of siRNAs, we prepared siRNAs targeting the green fluorescent protein (GFP) labeled with either fluorescent Alexa Fluor 647 (siRNA-alexa647) or 6-nm colloidal gold particles (siRNA-gold). The siRNAs were formulated in LNPs (final lipid/siRNA weight ratio ~10:1), as previously described[14]. The specific nanoparticles used in this study were prepared with the ionizable lipid DLin-MC3-DMA, disteroylphosphatidyl choline, cholesterol and PEG-DMG (molar ratio of ~50:10:38.5:1.5), using a spontaneous vesicle formation formulation procedure[7]. LNPs were then analyzed by light (**Fig. 1a**) and electron (**Fig. 1b**) microscopy (EM). Automated quantification of the preparations (~4,000 LNPs) of the EM images (**Supplementary Fig. 1a**) indicated that the average shape (**Supplementary Fig. 1b**) and size distribution (**Fig. 1c**) were not significantly altered in LNP formulations containing siRNAs conjugated to the fluorescent dye or the gold nanoparticles. We estimated the mean diameter of these LNPs to be ~60 nm, consistent with the size range for such particles determined by dynamic light scattering[14]. More than 80% of the particles had a diameter ranging from 40 nm to 120 nm that is optimal for silencing in the liver (A.A., unpublished data).

To determine whether the labeling had any effect on the knockdown efficiency of the siRNAs, we used an image-based assay to quantify the downregulation of GFP stably expressed in HeLa cells[19] (**Fig. 1d**). Dose-response experiments demonstrated efficient (~90%) downregulation of GFP at a concentration of 80 nM LNP-siRNA-gold (**Supplementary Fig. 1c**). At 20 nM concentration, the dose used previously *in vitro*[14], the efficacy of LNP-siRNA-alexa647 and LNP-siRNA-gold was comparable to LNPs containing the unlabeled siRNA (LNP-siRNA), reducing the GFP intensity by ~60–65% (**Fig. 1e**). With morphology and silencing efficiency very similar to those of the original formulation, the two traceable LNP platforms were deemed suitable for uptake and trafficking studies in cell culture as well as in livers of treated animals.

Kinetics and mechanisms of LNP uptake

To determine whether endocytosis is required for siRNA delivery and GFP downregulation, we tested the effect of dynasore. Dynasore is a small-molecule inhibitor of Dynamin[20], a GTPase required for membrane fission in clathrin-mediated endocytosis (CME) and other forms of internalization[21]. Dynasore treatment reduced the uptake of LNP-siRNA-alexa647 and transferrin by ~75% and ~90%, respectively, compared to control cells (**Fig. 2a**,**b**) and prevented the downregulation of GFP (**Fig. 2a**,**c**).

Based on the evidence that LNP internalization is dependent on LDLR[14], one would predict that it occurs by means of CME. To test this prediction, we first compared the kinetics of LNP uptake with those of low-density lipoprotein (LDL) (**Fig. 2d**). In contrast to the linear uptake kinetics of LDL (**Fig. 2e**, blue curve), the uptake of LNPs followed an exponential curve (**Fig. 2e**, red curve), suggesting that the uptake is biphasic. In the first phase (~1.5 h), LNPs entered cells with fast kinetics, similar to those of LDL endocytosis (**Supplementary Fig. 2a**). However, this accounts for only a small part of the total uptake (<1%) (**Fig. 2d** and **Supplementary Fig. 2b**). The second phase (2–6 h) accounts for 98% of the total uptake (**Fig. 2e**). These results raise the question of which endocytic mechanisms are responsible for the internalization of the majority of LNPs that enter the cells in the second phase.

To address this question, we downregulated key components of different endocytic mechanisms[21] (**Fig. 2f**). We observed a ~50% reduction of LNP uptake upon downregulation of clathrin heavy chain (CLTC), confirming a role for CME. Moreover, consistent with the reported ApoE- and LDLR-dependency[14], silencing of LDLR and LDL receptor-related protein 1 (LRP1) led to a 60–70% reduction in LNP uptake, whereas high-density lipoprotein (HDL) receptor (SRB1) downregulation had no effect. It is unlikely that the biphasic uptake was due to heterogeneous populations of LNPs containing siRNA and devoid of ApoE, because despite the initial low uptake the majority (65%) of LNPs did contain ApoE (**Supplementary Fig. 3**).

Downregulation of Caveolin 1 (CAV1), involved in caveolin-mediated endocytosis, did not modify LNP uptake. The knockdown of macropinocytosis regulators (CTBP1, Rac1, Rabankyrin-5)[21], but not of CDC42, which regulates the 'GPI-anchored protein-enriched early endocytic compartment/clathrin-independent carriers' (GEEC-CLIC), led to a ~60% decrease in LNP uptake (**Fig. 2f**). We further tested the requirement for macropinocytosis using a pharmacological inhibitor, ethylisopropylamiloride (EIPA). EIPA treatment reduced LNP uptake by ~70% (**Supplementary Fig. 2c**). HeLa cells exposed to LNPs displayed an approximately fourfold increased capacity of uptake of a fluid phase marker, 70-kDa dextran (**Supplementary Fig. 2d**

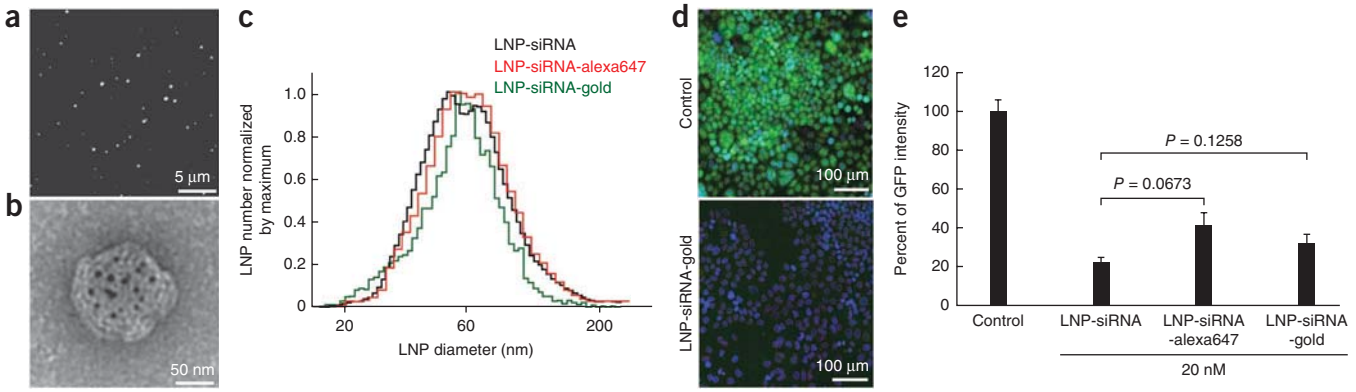

Figure 1 LNP-siRNA, LNP-siRNA-alexa647 and LNP-siRNA-gold have similar size and knock-down efficiency. (**a**,**b**) Visualization of LNP-siRNA-alexa647 and LNP-siRNA-gold by fluorescence (**a**) and electron microscopy (**b**). (**c**) Size distribution of LNP-siRNA, LNP-siRNA-alexa647 and LNP-siRNA-gold. (**d**) HeLa GFP cells control (upper panel) or 72 h after LNP-siRNA-gold (bottom panel). The red outlines correspond to the automated nucleus segmentation. (**e**) Quantification of GFP downregulation in HeLa GFP-expressing cells exposed to 20 nM of LNP-siRNA, LNP-siRNA-alexa647 and LNP-siRNA-gold ($n = 3$, mean ± s.e.m.).

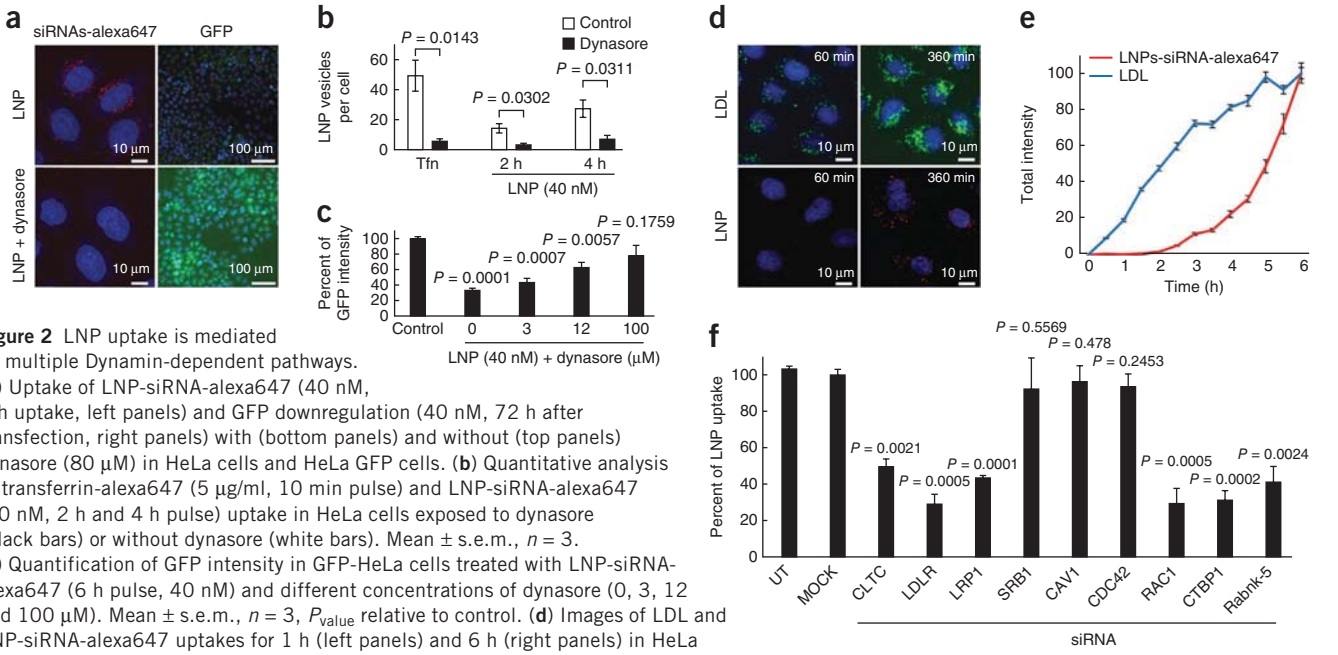

Figure 2 LNP uptake is mediated by multiple Dynamin-dependent pathways. (**a**) Uptake of LNP-siRNA-alexa647 (40 nM, 4 h uptake, left panels) and GFP downregulation (40 nM, 72 h after transfection, right panels) with (bottom panels) and without (top panels) dynasore (80 µM) in HeLa cells and HeLa GFP cells. (**b**) Quantitative analysis of transferrin-alexa647 (5 µg/ml, 10 min pulse) and LNP-siRNA-alexa647 (40 nM, 2 h and 4 h pulse) uptake in HeLa cells exposed to dynasore (black bars) or without dynasore (white bars). Mean ± s.e.m., $n = 3$. (**c**) Quantification of GFP intensity in GFP-HeLa cells treated with LNP-siRNA-alexa647 (6 h pulse, 40 nM) and different concentrations of dynasore (0, 3, 12 and 100 µM). Mean ± s.e.m., $n = 3$, P_{value} relative to control. (**d**) Images of LDL and LNP-siRNA-alexa647 uptakes for 1 h (left panels) and 6 h (right panels) in HeLa cells. (**e**) Uptake kinetics of LNP-siRNA-alexa647 (40 nM, red curve) compared to LDL-488 (3 µg/ml, blue curve). (**f**) LNP uptake in HeLa cells after silencing of key regulators of CME (CLTC, LDLR, LPR1 and SRB1), Caveolin-mediated endocytosis (CAV1), GEEC-CLIC pathways (CDC42) and Macropinocytosis (RAC1, CTBP1 and Rabankyrin-5). UT, untreated. Mean ± s.e.m., $n = 3$, P_{value} relative to control.

and **Supplementary Fig. 2e**), suggesting that LNPs themselves induce macropinocytosis (see below).

Inhibition of either CME or macropinocytosis reduced the uptake by 50–70% (depending on the siRNA and target genes, **Fig. 2f**), suggesting that both pathways are required. Simultaneous downregulation of both CLTC and the Rab5 effector Rabankyrin-5, a regulator of macropinosome biogenesis[22], did not have a significant additive effect (**Supplementary Fig. 2f**) as one could expect from independent processes. One possible interpretation is that CME is a prerequisite for macropinocytosis activation, as it is for the entry of adenovirus[23]. To test this hypothesis, we analyzed the formation of macropinosomes upon inhibition of CME. We found that silencing of CLTC

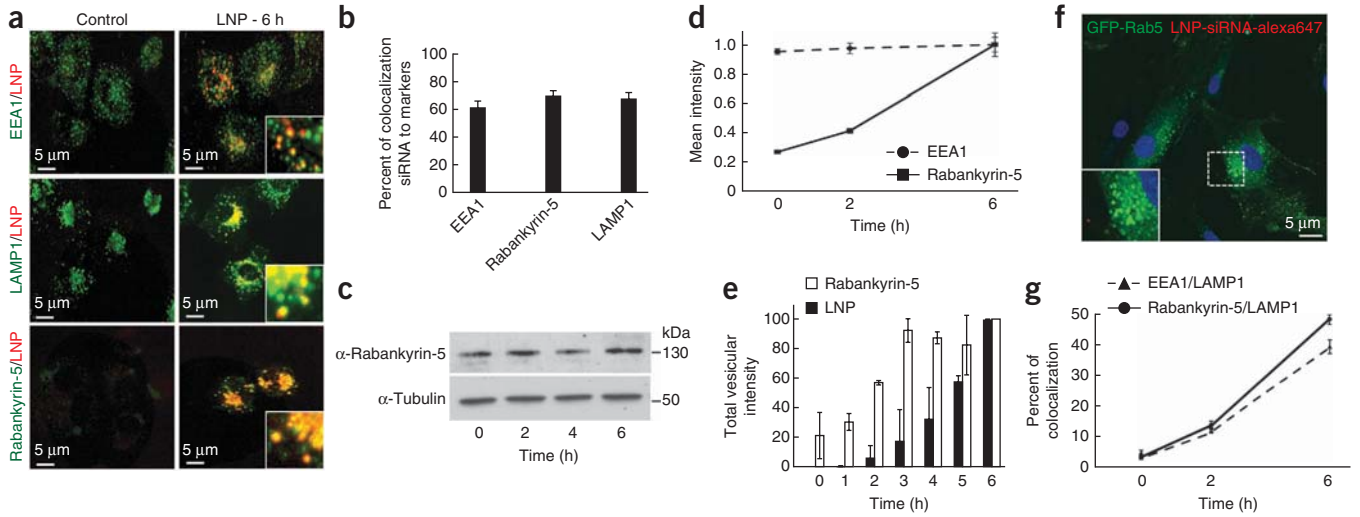

Figure 3 LNP uptake in HeLa cells induces the formation of a hybrid early-late endosomal compartment through recruitment of Rabankyrin-5. (**a**) HeLa cells incubated (right panels) or not (left panels) with LNP-siRNA-alexa647 (6 h pulse, 40 nM, red) were stained (green) with early endosome markers, EEA1 (top panel) and Rabankyrin-5 (bottom panel), or late endosome/lysosome marker, LAMP1 (middle panel) 6 h after LNP exposure. (**b**) Quantitative analysis of LNPs, EEA1, Rabankyrin-5 and LAMP1 colocalization 6 h after LNP exposure (mean ± s.e.m., $n = 3$). (**c**) Western-blot analysis of Rabankyrin-5 protein level upon LNP exposure (α-tubulin used as loading control, $n = 3$, $P = 0.2622$, 0.5377 and 0.8582 for 2, 4 and 6 h respectively). (**d**) Curves of the mean intensity of EEA1 (dashed line) and Rabankyrin-5 (black line) during LNP uptake, expressing the concentration of these markers per vesicle (mean ± s.e.m., $n = 3$) (**Supplementary Fig. 14**). (**e**) Quantitative analysis of the time-dependent total vesicular fluorescence intensity of Rabankyrin-5 (white columns) and LNPs (black columns). Mean ± s.e.m., $n = 3$. (**f**) Uptake of LNP-siRNA-alexa647 (6 h pulse, 40 nM, red) in primary human fibroblast expressing Rab5-GFP. (**g**) Analysis of EEA1/LAMP1 (dashed line) and Rabankyrin-5/LAMP1 (black line) co-localization during LNP uptake in HeLa cells (mean ± s.e.m., $n = 3$).

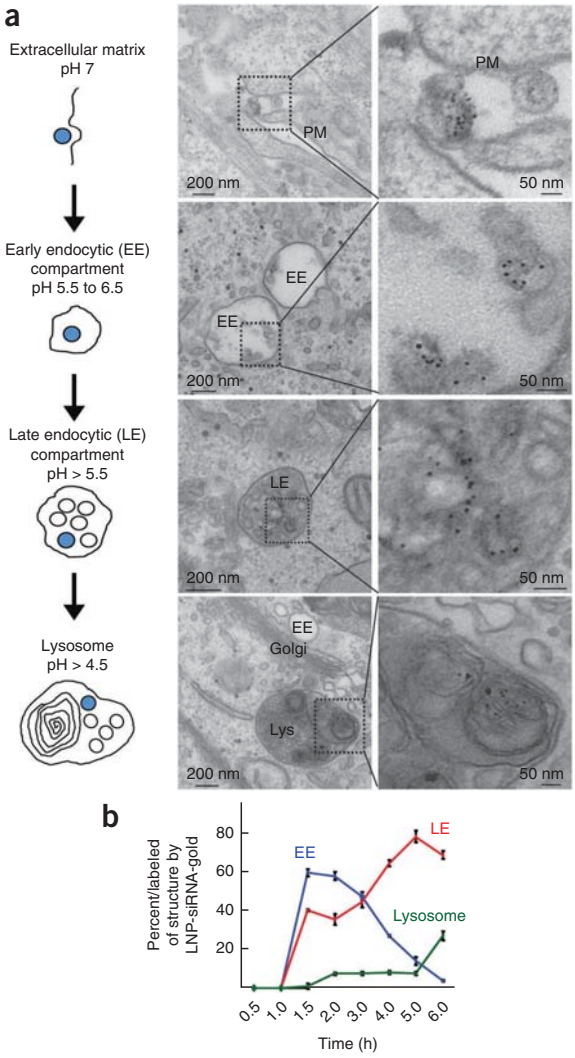

Figure 4 Ultrastructural analysis of LNP *in vitro* trafficking. (**a**) LNP-siRNA-gold detected in HeLa cells *in vitro*, by EM. LNP-siRNA-gold was found in the extracellular matrix close to the plasma membrane (PM) and inside early endocytic compartment (EE), late endocytic compartment (LE) and lysosome (Lys) within cells. Magnified images (right panels) permit appreciation of the suborganelle localization of siRNA-gold. (**b**) Time course of quantitative EM analysis of siRNA-gold progression within early endosomes (blue curve), late endosomes/MVBs (red curve) and lysosomes (green curve). Mean ± s.e.m., $n = 3$.

substantially reduced the formation of Rabankyrin-5–positive vesicles upon LNP exposure (**Supplementary Fig. 4a**), suggesting that macropinocytosis is activated following the uptake of LNPs by CME.

Next, we determined the contribution of both pathways to gene silencing. We measured the efficiency of GFP silencing after different times of LNP uptake followed by 72 h incubation (for GFP silencing). The first hour of uptake (by CME) resulted in ~10% of gene silencing (**Supplementary Fig. 2g**). The uptake from 2 h on (when macropinocytosis is induced and adds to CME) yielded the bulk of gene silencing activity. These results support the idea that macropinocytosis provides a major contribution to the uptake of LNP and gene silencing activity. Consistently, EIPA reduced by more than 60% the efficacy of silencing (**Supplementary Fig. 2d**).

Taken together, these results suggest that both CME and macropinocytosis contribute to LNP uptake and gene silencing. Macropinocytosis is induced following CME and is quantitatively the major delivery mechanism, as previously reported for other lipidoid-mediated siRNA delivery systems[9].

Recruitment of Rabankyrin-5 during LNP trafficking

We next explored the intracellular pathways of LNP trafficking and their underlying molecular requirements in HeLa cells. We observed a ~70% co-localization of LNPs with Rabankyrin-5 (**Fig. 3a**,**b**) 6 h after the cells' exposure to LNPs. As expected with the increased dextran uptake (**Supplementary Fig. 2e**), the number of Rabankyrin-5–positive vesicles increased greatly 6 h after incubation of cells with LNPs (**Fig. 3a**, right bottom panel), compared to untreated cells (**Fig. 3a**, left bottom panel). Notably, such increase was not due to an elevation of Rabankyrin-5 protein expression during LNP uptake (0 h, 1; 2 h, 1.09 ± 0.07; 4 h, 0.94 ± 0.07; 6 h, 1.04 ± 0.24; **Fig. 3c**). Instead, it was the amount of Rabankyrin-5 on membranes that progressively increased during the time course, demonstrating an augmented recruitment on LNP-containing vesicles (**Fig. 3d**).

Could the increased membrane recruitment of Rabankyrin-5 account for LNP uptake? Several lines of evidence support this hypothesis. First, the kinetics of membrane recruitment of Rabankyrin-5 paralleled those of LNP uptake (**Fig. 3e**). Second, downregulation of Rabankyrin-5 led to a ~60% reduction in LNP uptake (**Fig. 2f**). Third, the uptake of LNPs was constitutive (linear) in cells that contained Rabankyrin-5–positive vesicles, such as hepatocytes and NIH-3T3 (**Supplementary Fig. 5a–c**), and was triggered (exponential) in HeLa cells, which have very few Rabankyrin-5–positive vesicles (**Supplementary Fig. 5d**) under normal conditions. Human primary fibroblasts that contained few Rabankyrin-5–positive vesicles and poorly endocytosed 70-kDa dextran (**Supplementary Fig. 4b**) exhibited almost undetectable LNP uptake (**Fig. 3f**), and overexpression of Rabankyrin-5 or H-RasG12V, known to activate macropinocytosis[22,24], induced an increase in LNP uptake in these cells (**Supplementary Fig. 4b–d**). Altogether, these results suggest that LNP delivery is cell type–specific and LNPs can trigger their own uptake by a Rabankyrin-5-dependent process.

Biogenesis and maturation of LNP-containing organelles

What is the intracellular fate of LNP-containing compartments? Upon internalization, cargo is sequentially transported through early endosomes, late endosomes and lysosomes[25]. The various stages of transport can be evaluated by the time-dependent colocalization with specific markers such as early endosome antigen 1 (EEA1) for early endosomes and lysosomal-associated membrane protein 1 (LAMP1) for late endosomes and lysosomes. Unexpectedly, we measured a ~70% co-localization of LNPs with all three markers, Rabankyrin-5, EEA1 and LAMP1 (**Fig. 3a**, right panels and insets and **Fig. 3b**) after 6 h incubation. This high degree of colocalization was not an artifact of fixation as it was confirmed by live-cell imaging (**Supplementary Fig. 6**). Notably, we observed high (~50%) co-localization between EEA1 and LAMP1, and between Rabankyrin-5 and LAMP1 in cells incubated with LNPs (**Supplementary Fig. 7a**,**b**) compared to untreated cells (**Fig. 3g**).

To gain insights into the biogenesis of the LNP-containing compartments, we analyzed the co-localization of LNPs with Rabankyrin-5, EEA1 and LAMP1 over time. In untreated cells (**Fig. 3g**), the number of double co-localized structures was negligible (~4%). However, 6 h after cells' exposure to LNPs, the co-localization of LAMP1 with EEA1 or Rabankyrin-5 increased ~8- and ~14-fold, respectively, reaching ~50% of the population of LAMP1-positive vesicles. These results

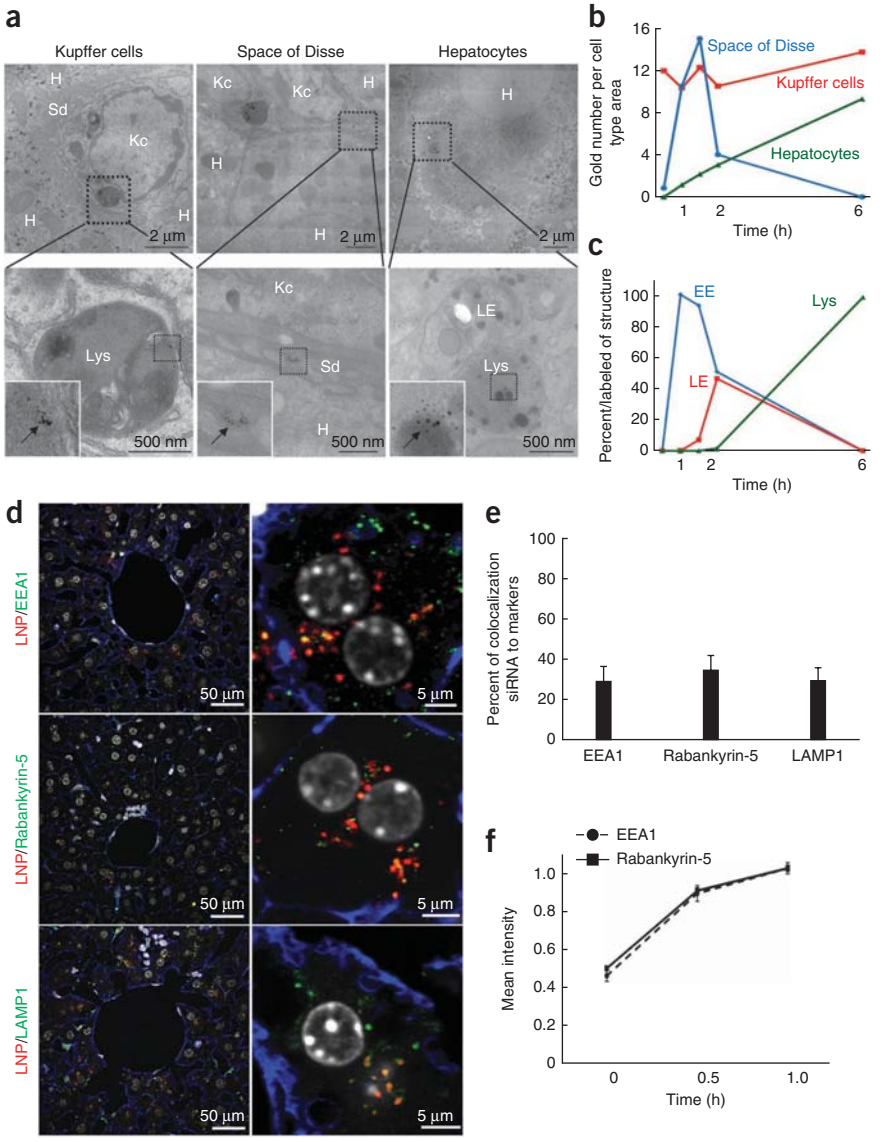

Figure 5 *In vivo* analysis of LNP bioavailability and intracellular trafficking. (**a**) EM analysis of LNP-siRNA-gold detection within Kupffer cells (Kc, left panels), the space of Disse (Sd, middle panels) and hepatocytes (H, right panels) after tail vein injection (Lys, lysosome and LE, late endocytic compartment). (**b**) Time course of quantitative EM analysis of LNP-siRNA-gold detection within Kupffer cells (red curve), the space of Disse (blue curve) and hepatocytes (green curve). Mean ± s.e.m. (**c**) Time course of quantitative EM analysis of siRNA-gold progression in hepatocytes within early (blue curve), late endocytic compartment (red curve) and lysosomes (green curve). Mean ± s.e.m., $n = 3$. (**d**) Liver sections from mice injected with LNP-siRNA-alexa647 (red) and immune-labeled for EEA1 (green, top panels), Rabankyrin-5 (green, middle panels) and LAMP1 (green, bottom panels). (**e**) Quantitative analysis of LNPs, EEA1, Rabankyrin-5 and LAMP1 colocalization 1 h after LNP exposure (mean ± s.e.m., $n = 3$). (**f**) Curves of mean intensity of EEA1 (dashed line) and Rabankyrin-5 (black line) upon LNPs uptake kinetics, expressing the concentration of these markers per vesicle (mean ± s.e.m., $n = 3$).

argue that the LNPs generate a hybrid compartment containing simultaneously early and late endocytic markers.

To further explore the nature of such an endosomal compartment, we examined its morphological features at the ultrastructural level in HeLa cells incubated with LNP-siRNA-gold for different periods of time. EM analysis (**Fig. 4a**) demonstrated that the majority of LNP-siRNA-gold particles were found within early endocytic structures and multivesicular bodies in the early phase of uptake (1.5 h). They were detected within lysosomes only 6 h after exposure of cells to LNPs (**Fig. 4b**). This is unexpected because we observed that the late endosome/lysosome marker LAMP1 had already co-localized with LNP-siRNA-alexa647 at 2 h (**Supplementary Fig. 7c**,**d**). Altogether these results indicate that siRNAs delivered with LNPs accumulated in a compartment having biochemical and morphological characteristics of both early and late endosomes and that matured slowly, thus delaying transport into lysosomes.

Bioavailability and intracellular trafficking of LNPs

Because the intracellular trafficking properties of LNPs and siRNAs in cultured cells were unanticipated and may have implications for siRNA escape, we validated these observations in a more relevant system *in vivo*. First, we dosed mice with LNPs containing siRNA-gold at therapeutically relevant concentrations (0.6 mg/kg) through tail vein injection[11] and inspected their bioavailability to the different cell types of the liver (**Fig. 5a**). We found that 30 min after tail vein injection, the endosomes and lysosomes of Kupffer cells, resident macrophages of the liver, were loaded with siRNA-gold (**Fig. 5b**). The LNPs were detected in the space of Disse 1 h after injection, concomitant with the onset of LNP uptake by hepatocytes (**Fig. 5b**). In hepatocytes, siRNA-gold was found in early and late endocytic compartments at 2 h and in lysosomes at 6 h (**Fig. 5c**). Consistent with the *in vitro* observations (**Supplementary Note** and **Supplementary Fig. 8**), the lysosomal marker LAMP1 was already detected at 1 h (**Fig. 5d**,**e**), demonstrating the delay in maturation of the hybrid early-late endosomal compartment. Moreover, we confirmed that the recruitment of Rabankyrin-5 was increased *in vivo* (**Fig. 5f**). The consistency between the data obtained in HeLa cells *in vitro* and hepatocytes *in vivo* suggests that the formation of Rabankyrin-5–positive structures is a key feature of LNP uptake and intracellular trafficking.

Quantification of siRNA escape

The escape of siRNA from endosomes into the cytosol is thought to be a rate-limiting step for many delivery approaches[26]. The lack of efficient methods to follow and quantify siRNA release from endosomes prevents (i) testing this hypothesis, (ii) gaining mechanistic insights into siRNA escape and (iii) developing the next generation of delivery systems for siRNA therapeutics. Recent studies have reported the detection of siRNA escape by light microscopy[15–18]. However, this requires much higher doses of LNPs, well above the therapeutic range.

We first used time-lapse confocal fluorescence microscopy to visualize the lifetime of compartments loaded with LNPs and capture

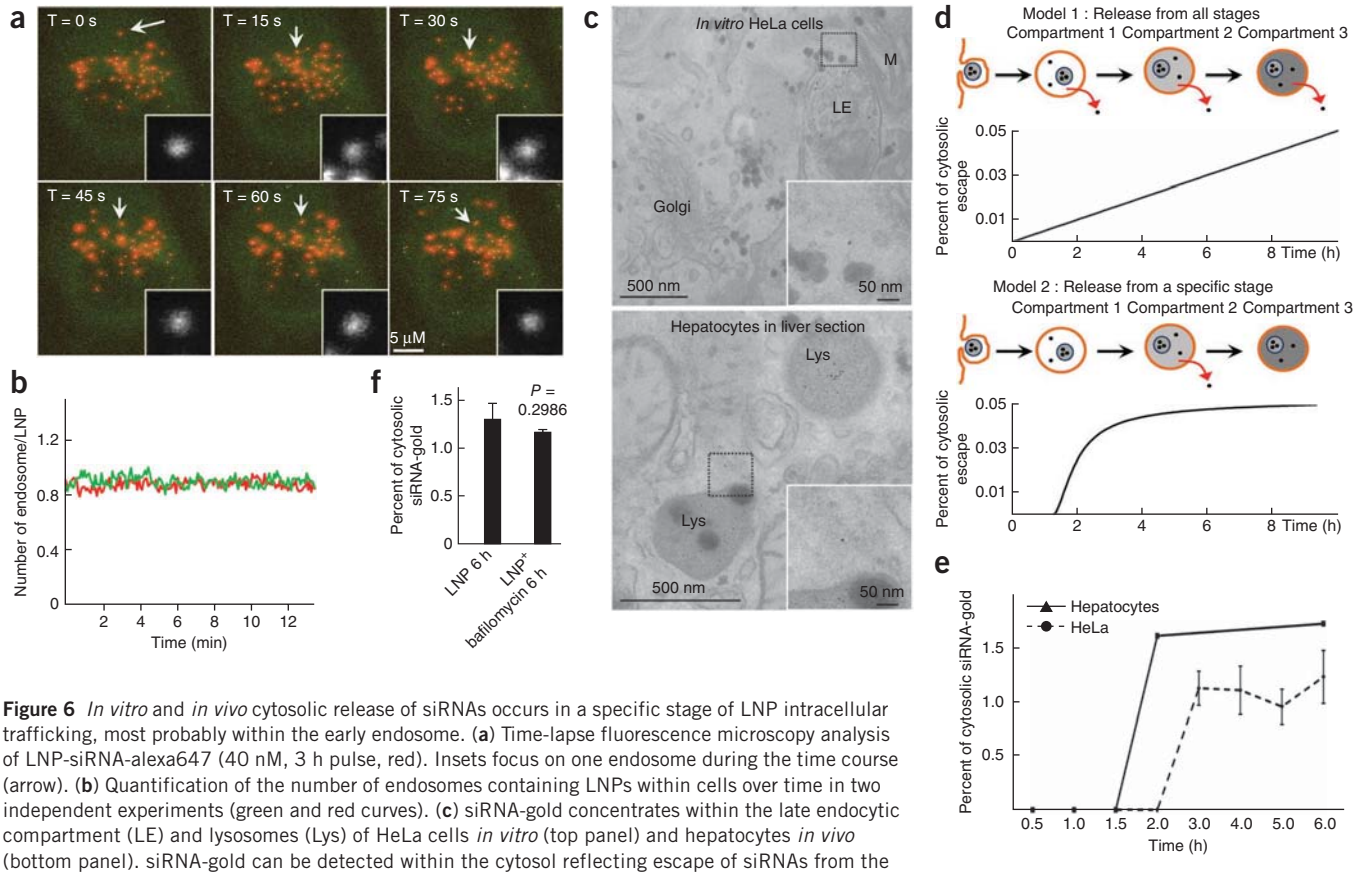

Figure 6 *In vitro* and *in vivo* cytosolic release of siRNAs occurs in a specific stage of LNP intracellular trafficking, most probably within the early endosome. (**a**) Time-lapse fluorescence microscopy analysis of LNP-siRNA-alexa647 (40 nM, 3 h pulse, red). Insets focus on one endosome during the time course (arrow). (**b**) Quantification of the number of endosomes containing LNPs within cells over time in two independent experiments (green and red curves). (**c**) siRNA-gold concentrates within the late endocytic compartment (LE) and lysosomes (Lys) of HeLa cells *in vitro* (top panel) and hepatocytes *in vivo* (bottom panel). siRNA-gold can be detected within the cytosol reflecting escape of siRNAs from the endolysosomal system (inset). (**d**) Mathematical modeling of siRNA escape from endosomes leads to two models in which the release occurs in all stages (top panel, linear curve) or in a specific stage (bottom panel, sigmoidal curve) of LNP intracellular trafficking. (**e**) Experimental results: quantification of cytosolic siRNA-gold release kinetics in liver section *in vivo* (black line) and in HeLa cells *in vitro* (dashed line). (**f**) Quantification of cytosolic siRNA-gold, with and without bafilomycin-A1 (2.5 µM, $n = 3$).

the release of siRNA into the cytosol. We observed that the vesicular compartments accumulating siRNAs were stable over long periods of time (**Fig. 6a**) and that their number and content did not significantly vary during the time course (**Fig. 6b**). These results argue that siRNAs delivered by LNPs at therapeutic doses are not massively released due to bursting of individual endosomes or permeabilization of the limiting membrane of endosomal compartments. More likely, the release is restricted to a limited number (a few hundreds) of siRNAs escaping from multiple endosomal compartments and undetectable by standard fluorescence microscopy methods.

To overcome this limitation, we analyzed cells loaded with LNP-siRNA-gold by EM. This approach allowed us to detect and semi-automatically quantify (**Supplementary Fig. 9**) the ratio of siRNA-gold within endosomal structures and in cytosol *in vitro* and *in vivo*. Our analysis yielded two important results. First, we could directly visualize siRNA-gold particles released into the cytosol (**Fig. 6c**). Because the siRNA-gold conjugates encapsulated in LNPs exhibit similar silencing activity to the unmodified LNP-siRNA, it appears that the presence of the 6-nm gold particles does not significantly affect intracellular trafficking and siRNA release. Second, we measured a low rate of escape. In HeLa cells, we estimated a release efficacy of 1.34 ± 0.08% leading to an escape of 249.8 ± 10.87 siRNA-gold per cell after 6 h (**Supplementary Note**). We found consistently that only 1.66 ± 0.07% of siRNA-gold escaped endosomes in hepatocytes *in vivo*, reaching 186.05 ± 10.51 siRNA-gold per cell after 6 h (**Supplementary Note**). These results are in agreement with the lack of detectable fluorescently labeled siRNAs in the cytosol by light microscopy (**Figs. 1**,**2**,**4**,**5** and **Supplementary Note**). In Kupffer cells, even when the endosomes and lysosomes were heavily loaded with LNPs (**Fig. 5a**,**b**), we were not able to detect siRNAs-gold in the cytosol, a result that correlates with the lack of silencing in these cells at these doses (W.Q. and A.B., unpublished data).

Naked siRNA-gold conjugates did not reach the cytosol and silence GFP under the same conditions (**Supplementary Fig. 10**). We cannot exclude the possibility that a fraction of siRNA-gold particle linkers were cleaved within the endosomes before release into the cytosol and, thus, escaped detection. However, it is important to note that the number of gold particles detected in the cytosol is in the range of the number of siRNAs previously estimated to be required for silencing[27]. Additionally, GFP silencing is highly correlated ($R^2 = 0.98$) with the estimated number of cytosolic siRNA-gold per cell in the linear phase of the curve (**Supplementary Fig. 11**). Furthermore, by Ago2 immunoprecipitation followed by STEM-Loop RT-PCR, it was shown that only about 3% of the total siRNAs were associated with the RISC complex 24 h after injection[28]. This value lies in a similar range as our estimate (1–2%). Our approach demonstrates that the lower silencing efficiency with a less active formulation (LNP-035) was predominantly due to a less efficient release of siRNA-gold from the endosomal compartment (**Supplementary Fig. 12a**,**b**), rather than reduced LNP uptake (**Supplementary Fig. 12a**,**c**), indicating that efficient uptake did not necessarily result in efficient gene silencing.

From which endosomal compartment do the siRNAs escape? To address this question, we first developed a mathematical model, based on ordinary differential equations to discriminate between a scenario in which the release occurs at a specific stage and one in which it occurs throughout the whole endolysosomal system (**Supplementary Note**). The model predicted different endosomal release kinetics for the two limiting cases for continuous internalization of LNPs. If the release of siRNAs occurred at all endosomal stages of LNP trafficking, cytosolic escape would be predicted to follow linear kinetics. By contrast, if the release occurred within a specific endosomal compartment, cytosolic escape should follow sigmoidal kinetics (**Fig. 6d**). We tested this model *in vitro* and *in vivo* by quantifying the ratio of cytosolic and total siRNA-gold during a time course and found that the release of siRNA-gold followed sigmoidal kinetics, arguing that siRNA escape occurs only at a specific stage of the endosomal trafficking of LNPs (**Fig. 6e**). The cytosolic release was not saturated by high doses of LNPs (**Supplementary Fig. 11c**), indicating that our experimental conditions were within the linear range. These results are consistent with the linearity previously observed between LNP dose and the number of RISC-loaded siRNAs[27,29].

To determine at which stage this release occurs, we blocked endosomal progression by using a pharmacological approach. Nocodazole treatment, well known to alter endosomal progression, did not inhibit GFP downregulation (**Supplementary Fig. 13a**). By contrast, bafilomycin treatment, which blocks endosomal acidification and inhibits progression of early to late endosomes (**Supplementary Fig. 13b–d**), inhibited LNP uptake but did not alter the efficiency of release of siRNA-gold (**Fig. 6f**). These results suggest that the siRNA release mainly occurred in a moderately acidic, early endocytic compartment.

DISCUSSION

In this study, we developed an analytical methodology to visualize LNP-mediated siRNA uptake, trafficking and escape from endosomes at therapeutically relevant concentrations. We used trackable particles and analyzed their distribution *in vitro* and *in vivo* using a combination of light microscopy and EM, quantitative image analysis and mathematical modeling. Our spatio-temporal analysis provides insights into the mechanisms, kinetics of cellular uptake and progression along the endosomal route, highlighting similarities and differences between cells *in vitro* and *in vivo*. We found that LNPs are internalized by a mechanism involving both CME and macropinocytosis. LNP uptake was inducible in HeLa cells by Rabankyrin-5-dependent macropinocytosis, in contrast to hepatocytes that constitutively internalized LNPs *in vivo*. An interesting finding of our quantitative analysis was that only a small fraction (1–2%) of siRNAs were released from endosomes and such release occurred only at a defined stage of endosomal progression. These findings suggest that the efficient delivery of functionally active siRNAs may be limiting even for state-of-the-art LNPs with excellent *in vivo* activity. Our results have the following important implications for the development of strategies to further improve the delivery of RNAi therapeutics.

Although LNP uptake clearly depends on receptor-mediated endocytosis[14], not all cells are equally competent for efficient and rapid LNP internalization. The delay of LNP uptake in the first 2 h observed for HeLa cells may, at least in part, be explained by the fact that the particles contain a polyethylene glycol (PEG)-lipid for steric stabilization during preparation and storage. The PEG shield is known to prevent or at least reduce the interaction of the particles with the cell surface and needs to be released for efficient cellular uptake. The PEG-lipid used here contained short (myristyl) tails, which allow for rapid exchange of the PEG-lipid *in vivo*[30,31]. However, deshielding of the particles in cell culture may be slower and hence delay the cellular uptake. In addition, such a difference in uptake between HeLa cells *in vitro* and hepatocytes *in vivo* could be explained by the recruitment of yet unidentified blood components that could accelerate uptake. Nevertheless, the kinetics of uptake in NIH3T3 cells, mouse hepatocytes in culture and *in vivo* are much faster than those in HeLa cells, suggesting that cell-specific mechanisms are key factors determining the mode of uptake. The exponential kinetics observed in HeLa cells for the LNPs analyzed in this study argue also in favor of a triggered process, consistent with macropinocytosis as an inducible entry mechanism. CME entry of LNPs seems to be a rate-limiting factor for macropinocytosis activation (**Supplementary Fig. 4a**). Our observations are reminiscent of adenovirus infection, where CME is the initial entry mechanism but subsequently triggers macropinocytosis[23]. Macropinocytosis is a highly flexible process allowing for the uptake of large volumes of fluid and high molecular weight molecules (e.g., 70-kDa dextran) and has been previously shown to be involved in other lipidoid-mediated siRNA delivery[9]. Our results suggest that modulation of cellular uptake of LNPs (receptor binding, mode of entry) is one of the areas that may allow for further improvements. As shown previously, the use of specific targeting ligands can deliver LNPs to target tissue independent of endogenous delivery mechanisms[14]. This may be of particular interest for targeting extrahepatic cells and tissues.

Endosomal trafficking is a second area of potential improvement. We demonstrated that LNPs concentrated in a slowly maturing, hybrid early-late endocytic compartment. Strong EEA1 and LAMP1 colocalization has been found associated with an arrest of early endosomal maturation in murine cytomegalovirus-infected cells[32]. Our data are consistent with escape occurring mainly from an early endocytic structure before transport to late endosomes/lysosomes. Escape may also occur from macropinosomes, as they have been attributed a high rate of leakiness[23]. The mechanism leading to the formation of an early-late hybrid endocytic compartment is still unknown. Ionizable lipids could interact with the endosomal lipids or alter the luminal pH, leading to alteration in the machinery underlying endosomal conversion[33] and transport to lysosomes, for example, SAND1/Mon1 (ref. 34). Retarding the progression of the LNPs along the endocytic pathway or diverting more of the material to the macropinocytic pathway may be one possible area of intervention to improve the efficacy of siRNA release.

Our findings suggest that only a very minor fraction (1–2%) of siRNAs were released from endosomes. We found only ~200 cytosolic siRNA-gold per cell at 6 h both *in vitro* and *in vivo*. With an average of 10–20 siRNA molecules per gold particle, this amounts to a maximum of 2,000–4,000 siRNA molecules per cell, which is in the range of the estimated levels of functionally active siRNAs interacting with the RISC per cell at therapeutically relevant concentration[29,35]. This explains why, in contrast to previous reports[15–18], we were unable to detect siRNA escape by fluorescence microscopy methods. Our observation is reinforced by earlier work[36], demonstrating that siRNA-FITC, which appear as bright concentrated dots when loaded in endosome, become undetectable after endosomes burst owing to dilution into cytosol[36]. We estimated that at least 20,000 cytosolic siRNAs are required to visualize a diffuse (cytosolic) fluorescence signal in HeLa cells (~115,000 in hepatocytes) under the detection limit of our confocal microscopy set-up (**Supplementary Note**), both far above the ~200 cytosolic siRNA-gold particles detected in our EM analysis.

These results raise the question of the mechanisms whereby siRNAs escape from endosomes to reach RISC in the cytosol.

Several lines of evidence are inconsistent with the "proton sponge" effect, a commonly proposed mechanism for LNP-based siRNA delivery[26]. First, we could not detect endosomes bursting during LNP trafficking by live cell imaging. Second, the gold-siRNAs were concentrated within a closed bilayer membrane. Third, bafilomycin, an inhibitor of vacuolar-type H^+-ATPase (V-ATPase), did not alter the release of siRNA-gold. However, our findings are consistent with the mechanism of lipid exchange and ion pair formation between the ionizable lipid and negatively charged lipid components of the endosomal membrane during acidification of the endosome[37] and the importance of the acid dissociation constant (pK_a) of the ionizable lipids for efficient siRNA delivery, with an optimum pK_a between 6.2–6.5 (ref. 7). On the other hand, it cannot be ruled out that lipid-independent mechanisms participate in the siRNA escape from endosomes as suggested by the fact that naked siRNA, siRNA-GalNAc and siRNA-IgG have been reported to downregulate genes *in vivo*[38–40]. One could consider low-throughput siRNA channels or transporters[41,42] as potential low efficiency release mechanisms. However, our observation that siRNAs-gold particles, estimated as above >8 nm, escaped endosomes and were active in gene silencing suggest a mechanism that is not restricted to the size of single siRNA duplexes. This suggests that endosomes are to some extent leaky to content escape, as observed in cell-free systems[43,44].

By demonstrating that escape from endosomes is a key rate-limiting step in siRNA efficiency, we propose that this provides the major opportunity to improve the delivery system. Strategies to enhance siRNA release and improve silencing efficiency *in vivo* may require further optimization of LNP composition and could involve the utilization of additional membrane-active components, such as cell-penetrating peptides[45,46], or lipid components, which facilitate siRNA release from the carrier. Moreover, one promising approach could be to generate bio-inspired LNPs by incorporating molecular features of exosomes to harness cell-catalyzed endosomal fusion mechanisms[47]. Furthermore, because we demonstrated that the release occurs in a specific stage of LNP endosomal trafficking, the siRNA discharge from LNP lipids could also be seen as a rate-limiting factor for silencing efficacy. Indeed, permanently charged lipids or inducible lipids with higher pK_a could impede siRNA discharge in the endosomal release window. Therefore, our results point at the importance of carefully selecting the lipid composition of the LNPs. Nonetheless, to select and validate formulations for their potential to improve siRNA release, reliable methods to quantify siRNA in various subcellular compartments are required. In this respect, our methodological approach can serve as an accurate analytical method to achieve this goal.

METHODS

Methods and any associated references are available in the online version of the paper.

Note: Supplementary information is available in the online version of the paper.

ACKNOWLEDGMENTS

We acknowledge T. Galvez and E. Perini for discussions and comments on the manuscript. We thank J.-M. Verbavatz and J. Peychl, respectively, for the management of the Electron Microscopy Facility and the Light Microscopy Facility. We thank A. Giner for cell culture, W. John and A. Muench-Wuttke from the Biomedical Service Facility for mouse care and injections, A. Pal and R. Villasenor for Rab5-GFP primary human fibroblasts and H-RasG12V cells preparation. We thank D. Butler, R. Kallanthottathil and M. Manoharan for advice on chemistry. This work was financially supported by the Max Planck Society (M.P.G.), the Virtual Liver initiative (http://www.virtual-liver.de) funded by the German Federal Ministry of Research and Education (BMBF), the DFG and Alnylam Pharmaceuticals. J.G. was supported by a grant from EMBO long-term fellowship.

AUTHOR CONTRIBUTIONS

M.Z. conceived and directed the project. M.Z., J.G., V.K., A.Z., W.Q., A.A., A.B., K.F., M.M. and Y.K. designed the experiments. M.M. synthesized the siRNA-gold conjugates. L.Z. synthesized the siRNA-alexa647. H.E.-B. formulated LNPs. C.A. and U.S., under the supervision of J.G., A.Z., E.F. and M.B., performed the *in vitro* fluorescence microscopy staining. M.S. performed the OPERA automated image acquisitions. G.M., under the supervision of Y.K., provided the quantitative multi-parametric image analysis and the statistics. A.Z. and S.S. directed the mouse tail-vein injections and the liver perfusion. J.G. and A.Z. co-developed the staining procedures for the tissues sections. J.G. performed the sections, staining and imaging. J.G. helped by K.M. developed the quantitative electron microscopy. Y.K. developed the mathematical model of siRNA cytosolic release. G.M. developed the software for automated counting of gold number on electron microscopy images. M.Z., J.G., W.Q., Y.K. and M.M. wrote the manuscript.

COMPETING FINANCIAL INTERESTS

The authors declare competing financial interests: details are available in the online version of the paper.

1. Vaishnaw, A.K. *et al.* A status report on RNAi therapeutics. *Silence* **1**, 14 (2010).
2. Czech, B. & Hannon, G.J. Small RNA sorting: matchmaking for Argonautes. *Nat. Rev. Genet.* **12**, 19–31 (2011).
3. Sliva, K. & Schnierle, B.S. Selective gene silencing by viral delivery of short hairpin RNA. *Virol. J.* **7**, 248 (2010).
4. Shim, M.S. & Kwon, Y.J. Efficient and targeted delivery of siRNA in vivo. *FEBS J.* **277**, 4814–4827 (2010).
5. Zhang, S., Zhao, Y., Zhi, D. & Zhang, S. Non-viral vectors for the mediation of RNAi. *Bioorg. Chem.* **40**, 10–18 (2012).
6. Semple, S.C. *et al.* Rational design of cationic lipids for siRNA delivery. *Nat. Biotechnol.* **28**, 172–176 (2010).
7. Jayaraman, M. *et al.* Maximizing the potency of siRNA lipid nanoparticles for hepatic gene silencing *in vivo*. *Angew. Chem. Int. Edn Engl.* **51**, 8529–8533 (2012).
8. Frank-Kamenetsky, M. *et al.* Therapeutic RNAi targeting PCSK9 acutely lowers plasma cholesterol in rodents and LDL cholesterol in nonhuman primates. *Proc. Natl. Acad. Sci. USA* **105**, 11915–11920 (2008).
9. Love, K.T. *et al.* Lipid-like materials for low-dose, in vivo gene silencing. *Proc. Natl. Acad. Sci. USA* **107**, 1864–1869 (2010).
10. Akinc, A. *et al.* A combinatorial library of lipid-like materials for delivery of RNAi therapeutics. *Nat. Biotechnol.* **26**, 561–569 (2008).
11. Zeigerer, A. *et al.* Rab5 is necessary for the biogenesis of the endolysosomal system in vivo. *Nature* **485**, 465–470 (2012).
12. Trial to Evaluate Safety and Tolerability of ALN-PCS02 in Subjects With Elevated LDL-Cholesterol (LDL-C). NCT01437059 (Registry of Federally and Privately Supported Clinical Trials, U.S. National Institutes of Health, 2011.
13. Trial to Evaluate Safety, Tolerability, and Parmacokinetics of ALN-TTR02 in Healthy Volunteer Subjects. NCT01559077 (Registry of Federally and Privately Supported Clinical Trials, US National Institutes of Health, 2012.
14. Akinc, A. *et al.* Targeted delivery of RNAi therapeutics with endogenous and exogenous ligand-based mechanisms. *Mol. Ther.* **18**, 1357–1364 (2010).
15. Basha, G. *et al.* Influence of cationic lipid composition on gene silencing properties of lipid nanoparticle formulations of siRNA in antigen-presenting cells. *Mol. Ther.* **19**, 2186–2200 (2011).
16. Tamura, A., Oishi, M. & Nagasaki, Y. Enhanced cytoplasmic delivery of siRNA using a stabilized polyion complex based on PEGylated nanogels with a cross-linked polyamine structure. *Biomacromolecules* **10**, 1818–1827 (2009).
17. Akita, H. *et al.* Nanoparticles for ex vivo siRNA delivery to dendritic cells for cancer vaccines: programmed endosomal escape and dissociation. *J. Control. Release* **143**, 311–317 (2010).
18. Sakurai, Y. *et al.* Endosomal escape and the knockdown efficiency of liposomal-siRNA by the fusogenic peptide shGALA. *Biomaterials* **32**, 5733–5742 (2011).
19. Bramsen, J.B. *et al.* A large-scale chemical modification screen identifies design rules to generate siRNAs with high activity, high stability and low toxicity. *Nucleic Acids Res.* **37**, 2867–2881 (2009).
20. Macia, E. *et al.* Dynasore, a cell-permeable inhibitor of dynamin. *Dev. Cell* **10**, 839–850 (2006).
21. Doherty, G.J. & McMahon, H.T. Mechanisms of endocytosis. *Annu. Rev. Biochem.* **78**, 857–902 (2009).
22. Schnatwinkel, C. *et al.* The Rab5 effector Rabankyrin-5 regulates and coordinates different endocytic mechanisms. *PLoS Biol.* **2**, e261 (2004).
23. Meier, O. *et al.* Adenovirus triggers macropinocytosis and endosomal leakage together with its clathrin-mediated uptake. *J. Cell Biol.* **158**, 1119–1131 (2002).
24. Schmees, C. *et al.* Macropinocytosis of the PDGF beta-receptor promotes fibroblast transformation by H-RasG12V. *Mol. Biol. Cell* **23**, 2571–2582 (2012).
25. Gruenberg, J. & Maxfield, F.R. Membrane transport in the endocytic pathway. *Curr. Opin. Cell Biol.* **7**, 552–563 (1995).

26. Dominska, M. & Dykxhoorn, D.M. Breaking down the barriers: siRNA delivery and endosome escape. *J. Cell Sci.* **123**, 1183–1189 (2010).
27. Pei, Y. *et al.* Quantitative evaluation of siRNA delivery in vivo. *RNA* **16**, 2553–2563 (2010).
28. Maier, M. in 8th Annual Meeting of the Oligonucleotide Therapeutics Society, Boston. (2012).
29. Wei, J. *et al.* RNA-induced silencing complex-bound small interfering RNA is a determinant of RNA interference-mediated gene silencing in mice. *Mol. Pharmacol.* **79**, 953–963 (2011).
30. Romberg, B., Hennink, W.E. & Storm, G. Sheddable coatings for long-circulating nanoparticles. *Pharm. Res.* **25**, 55–71 (2008).
31. Wheeler, J.J. *et al.* Stabilized plasmid-lipid particles: construction and characterization. *Gene Ther.* **6**, 271–281 (1999).
32. Tomas, M.I., Kucic, N., Mahmutefendic, H., Blagojevic, G. & Lucin, P. Murine cytomegalovirus perturbs endosomal trafficking of major histocompatibility complex class I molecules in the early phase of infection. *J. Virol.* **84**, 11101–11112 (2010).
33. Rink, J., Ghigo, E., Kalaidzidis, Y. & Zerial, M. Rab conversion as a mechanism of progression from early to late endosomes. *Cell* **122**, 735–749 (2005).
34. Poteryaev, D., Datta, S., Ackema, K., Zerial, M. & Spang, A. Identification of the switch in early-to-late endosome transition. *Cell* **141**, 497–508 (2010).
35. Landesman, Y. *et al.* In vivo quantification of formulated and chemically modified small interfering RNA by heating-in-Triton quantitative reverse transcription polymerase chain reaction (HIT qRT-PCR). *Silence* **1**, 16 (2010).
36. Lee, S.H., Choi, S.H., Kim, S.H. & Park, T.G. Thermally sensitive cationic polymer nanocapsules for specific cytosolic delivery and efficient gene silencing of siRNA: swelling induced physical disruption of endosome by cold shock. *J. Control. Release* **125**, 25–32 (2008).
37. Hafez, I.M., Maurer, N. & Cullis, P.R. On the mechanism whereby cationic lipids promote intracellular delivery of polynucleic acids. *Gene Ther.* **8**, 1188–1196 (2001).
38. Lewis, J. *et al.* In vivo silencing of alpha-synuclein using naked siRNA. *Mol. Neurodegener.* **3**, 19 (2008).
39. Hauser, P.V. *et al.* Novel siRNA delivery system to target podocytes in vivo. *PLoS ONE* **5**, e9463 (2010).
40. Xia, C.F., Boado, R.J. & Pardridge, W.M. Antibody-mediated targeting of siRNA via the human insulin receptor using avidin-biotin technology. *Mol. Pharm.* **6**, 747–751 (2009).
41. Valiunas, V. *et al.* Connexin-specific cell-to-cell transfer of short interfering RNA by gap junctions. *J. Physiol. (Lond.)* **568**, 459–468 (2005).
42. Wolfrum, C. *et al.* Mechanisms and optimization of in vivo delivery of lipophilic siRNAs. *Nat. Biotechnol.* **25**, 1149–1157 (2007).
43. Ohya, T. *et al.* Reconstitution of Rab- and SNARE-dependent membrane fusion by synthetic endosomes. *Nature* **459**, 1091–1097 (2009).
44. Starai, V.J., Jun, Y. & Wickner, W. Excess vacuolar SNAREs drive lysis and Rab bypass fusion. *Proc. Natl. Acad. Sci. USA* **104**, 13551–13558 (2007).
45. Andaloussi, S.E. *et al.* Design of a peptide-based vector, PepFect6, for efficient delivery of siRNA in cell culture and systemically in vivo. *Nucleic Acids Res.* **39**, 3972–3987 (2011).
46. Bartz, R. *et al.* Effective siRNA delivery and target mRNA degradation using an amphipathic peptide to facilitate pH-dependent endosomal escape. *Biochem. J.* **435**, 475–487 (2011).
47. Kobayashi, T. *et al.* The tetraspanin CD63/lamp3 cycles between endocytic and secretory compartments in human endothelial cells. *Mol. Biol. Cell* **11**, 1829–1843 (2000).

ONLINE METHODS

Animals. All animal studies were conducted in accordance with German animal welfare legislation and in strict pathogen-free conditions in the animal facility of the Max Planck Institute of Molecular Cell Biology and Genetics, Dresden, Germany. Protocols were approved by the Institutional Animal Welfare Officer (Tierschutzbeauftragter), and necessary licenses were obtained from the regional Ethical Commission for Animal Experimentation of Dresden, Germany (Tierversuchskommission, Landesdirektion Dresden). All procedures used in animal studies conducted at Alnylam Pharmaceuticals were approved by the Institutional Animal Care and Use Committee and were consistent with local, state and federal regulations as applicable. C57BL/6NHsd 8–12 weeks old male mice (Harlan laboratories) were injected with 0.6 mg/kg of LNP-siRNA-gold or LNP-siRNA-alexa647 by tail vein injection. For EM analysis, after 0.5, 1, 1.5, 2 and 6 h after injection, mice were euthanized using cervical dislocation and liver was harvested and fixed in glutaraldehyde. For immunofluorescence analysis, after 0.5 and 1 h after injection, mice were first perfused with paraformaldehyde 4% for 30 min before liver collection.

Antibodies and reagents. Rabbit anti-EEA1 and rabbit anti-Rabankyrin-5 were developed in our laboratory as previously described[22]. Rat anti-LAMP1 antibody was purchased from BD Bioscience (Heidelberg, Germany). Goat anti-rabbit and goat anti-rat secondary antibodies, labeled, respectively, with Alexa Fluor 488 and Alexa Fluor 555, were obtained from Molecular Probes, Europe. Dynasore, Nocodazole, bafilomycin A1 and EIPA were purchased from Sigma-Aldrich Biochemie (Hamburg, Germany). ApoE was obtained from Fitzgerald (Acton, MA, USA). Transferrin conjugated to Alexa Fluor 647 was purchased from Molecular Probes, Europe. LDL was purified from human serum and labeled with Alexa Fluor 488 as previously described[33]. Large Dextran (70 kDa) was obtained from Invitrogen. FITC-labeled ApoE was made at Alnylam.

siRNA modification and formulation into lipid nanoparticles. The siRNAs used in this study target GFP (eGFP plasmid, Clonetech). The unconjugated siRNA-1 consisted of a 19 basepair duplex with two-nucleotide overhangs on both ends: sense 5′-AcAuGAAGcAGcACGACuUdT*dT; antisense: 5′-AAGUCGUGCUGCUUCAUGUdT*dT. The siRNA used for fluorescent microscopy studies (siRNA-2) was labeled at the 3′-end of the antisense strand with Alexa Fluor 647: antisense: 5′-AAGUCGUGCUGCUUCAUGUd TdTL48. For conjugation to gold nanoparticles, the sense strand of siRNA-3 contained an extended 3′-overhang carrying disulfide functionality: sense 5′-AcAuGAAGcAGcACGACuUdTdTdTdTdTdTdTdTdTdTdTQ51dT. The lower-case letters represent 2′-*O*-methyl-modified nucleotides, asterisks represent phosphorothioate linkages, L48 represents Alexa Fluor 647 conjugated to a 4-hydroxyprolinol-based linker and Q51 represents 6-((6-hydroxyhexyl) disulfanyl)hexyl phosphate. RNA oligonucleotides were synthesized using commercially available 5′-*O*-(4,4′-dimethoxytrityl)- 2′-*O*-t-butyldimethylsilyl-3′-*O*-(2-cyanoethyl-N,N-diisopropyl)-protected phosphoramidite monomers of uridine, 4-*N*-acetylcytidine, 6-*N*-benzoyladenosine and 2-*N*-isobutyrylguanosine and the corresponding 2′-*O*-methyl phosphoramidites according to standard solid-phase oligonucleotide synthesis protocols[48]. The crude oligonucleotides were analyzed by liquid chromatography–mass spectrometry, purified by anion-exchange high-performance liquid chromatography (IEX-HPLC) and desalted by size-exclusion chromatography, as described previously[49,50]. siRNA duplexes were prepared by annealing equal molar amounts of sense and antisense strands in PBS buffer[50]. For the antisense strand labeled with Alexa Fluor 647, a precursor oligonucleotide carrying a primary amino group at its 3′-end was synthesized on controlled pore glass support preloaded with a 4-hydroxyprolinol-based linker bearing two orthogonally protected reactive sites, a primary hydroxy group for oligonucleotide synthesis and a primary amino group for conjugation[51]. After deprotection, the amine-containing precursor oligonucleotide was purified and desalted. To the precursor dissolved at a concentration of ~1 mM in 0.1 M sodium tetraborate buffer (pH = 8.5), we added four equivalents of the Alexa Fluor 647 NHS ester (Life Technologies) in DMSO (~30% of the volume of the aqueous RNA solution) and the mixture was shaken at room temperature for 3 h before the crude conjugate was purified by IEX-HPLC and desalted. For the sense strand carrying the disulfide functionality, the Thiol-Modifier C6 S-S (Glen Research) was introduced by phosphoramidite chemistry according to the manufacturer's protocol.

Gold nanoparticles (AuNPs) conjugated with siRNA were prepared using a procedure modified from previously reported protocols (**Supplementary Methods**). In a typical preparation, 200 mg of bis-(*p*-sulfonatophenyl)pheny lphosphine dihydrate dipotassium salt (BSPP, Sigma-Aldrich) were added to 200 ml of AuNP solution (6 nm Gold Sol, Aurion) and the mixture was gently shaken for 12–16 h at room temperature. The solution was transferred to 50-ml centrifuge tubes and the gold was precipitated by adding solid NaCl to a final concentration of 1 M. After vortexing, the color of mixture changed from red to a cloudy purple and the precipitated gold was collected by centrifugation at 3,500 r.p.m. for 15 min and removal of the supernatant. The pellets were resuspended in BSPP buffer (1 mg/ml BSPP in deionized water) to a final particle concentration of about 3–4 µM and 1.2 equiv. of disulfide-modified siRNA-3 was added based on the maximal loading capacity calculated according to the following equation (**Supplementary Methods**):

$$mol\,conjugated\,oligonucleotide = 4\pi r^2 \times C(Au) \times 35\,pmol/cm^2 \times V$$

where r is the radius of the nanoparticles, $C(Au)$ is the concentration of AuNPs determined spectrophotometrically at 520 nm using an extinction coefficient ε(520) of $1 \times 10^7\ M^{-1}cm^{-1}$, and V is the volume of the nanoparticle solution (in liters).

After gently shaking the mixture with for about 24 h at room temperature, the crude Au-siRNA conjugates were purified by reversed phase HPLC on a DeltaPak C_{18} column (7.8 × 250 mm) using 0.05 M triethylammonium acetate buffer, pH 7 (A) and acetonitrile (B) and a gradient of 0–40% B in 35 min. Product-containing fractions were combined, reduced to a volume of about 10 ml and desalted on a Sephadex G-25 column. After reducing the volume to about 3–5 ml, the final concentration of Au nanoparticles was determined as described above. The siRNA concentration was determined spectrophotometrically by measuring the absorbance at 260 nm after treating an aliquot of the Au-siRNA conjugate solution with an equal volume of 30 mM KCN solution in water at 45 °C for 1.5 h. A sample containing equally concentrated unconjugated AuNP treated identically with KCN solution served for baseline adjustment. Typically, the siRNA/Au ratio ranged between 10–20 siRNAs per particle.

Modified and unmodified siRNA were incorporated in lipid nanoparticles as published previously[6]. Nanoparticles were prepared with the ionizable lipid, disteroylphosphatidyl choline, cholesterol, and PEG–DMG using a spontaneous vesicle formation formulation procedure. Lipids were dissolved in 90% ethanol solution and mixed with siRNA solution (10 mM citrate, pH 3) at fixed speed; 1:3 with labeled Alexa Fluor siRNA and 1:5 ratio for AuNPs-siRNA. The ethanol was then removed and the external buffer replaced with PBS (155 mM NaCl, 3 mM Na_2HPO4, 1 mM KH_2PO_4, pH 7.5) by dialysis. The particles had a component molar ratio of ~50:10:38.5:1.5 (ionizable lipid/disteroylphosphatidyl choline/cholesterol/PEG–DMG). The final lipid/siRNA weight ratio was ~10:1. Particle size were determined using a Malvern Zetasizer NanoZS (Malvern, UK), AuNPs-siRNA were sized before formulation (~20 nm) and after formulation in LNP (100–130 nm). For AuNPs-siRNA LNP content was determined spectrophotometrically by measuring the absorbance at 520 nm after treating an aliquot of the LNP solution with an equal volume of Triton-X100 solution (2% in water), vortexing and incubating at 37 °C for 10 min. For labeled Alexa Fluor-siRNA, LNP siRNA content was determined by ion exchange HPLC (Agilent) assay using DNAPac Pa200 column (Dionex Corporation Dionex, 260 nm, 55 °C run at 2 ml/min).

LNP characterization. LNP shape and size distributions were analyzed by EM. LNP solutions were added on the surface of carbon-coated grids for 5 min. The grids were rinsed quickly and incubated for 30 s with 2% uranyl acetate in water. Images were acquired at 11,000× magnification on a Tecnai 12 TEM microscope (FEI) (electron microscopy facility, MPI-CBG, Dresden). By using MotionTracking software, individual LNPs were identified by fitting analysis. Indeed, the image intensity was fitted by a sum of powered Lorenzian functions, as previously described[33]. Objects displaying unreliable features, such as low intensity and excessive elongation, were filtered out by a set of manually adjusted filters, chosen to maximize the number of true liposome

doi:10.1038/nbt.2612

structures considered for the following analysis, and at the same time minimize the number of false liposome structures. At least 4,000 LNPs per condition were counted. The size distribution was then fitted to a Gaussian distribution, to estimated mean value and dispersion of liposome size. Moreover, for each individual structure detected, multiparametrics coefficients were calculated to describe the shape of these LNPs (e.g., size, intensity, intensity volume, elongation).

To determine the amount of ApoE loaded on LNPs, we incubated LNP-siRNA-alexa647 with ApoE-FITC (3 µg/ml) for 1 h at room temperature, before gelatin embedding and confocal imaging.

Gold-labeled siRNA were detected easily by EM on sample stained by negative staining. LNPs formulated with alexa-647 labeled siRNA were entrapped in 12% gelatin between glass slide and cover slip and imaged on a spinning disc fluorescent microscope (light microscopy facility, MPI-CBG, Dresden).

Cell culture, cell lines and transfections. HeLa Kyoto, GFP-HeLa cells[19] and GFP-NIH3T3 were cultured in DMEM media complemented with 10% FBS and 1% penicillin-streptomycin at 37 °C and 5% CO_2. When required cells were seeded on 24- (for EM analysis) or 96- (for fluorescence microscopy analysis) well plates. Hepatocytes, from wild-type and GFP-expressing mice, were purified and cultured as described in **Supplementary Methods**. For transfection, LNP solution was mixed with ApoE (3 µg/ml) in DMEM containing serum and added on the cells. Primary human fibroblasts (GM00041), obtained from Coriell Institute, were cultured and transfected with YFP-Ranbankyrin-5 (Lipofectamin) or infected with Rab5-GFP as described in supplementary METHODS. H-RasG12V fibroblasts were cultured and used for dextran uptake as previously described[24]. HeLa-GFP-Rab5 and HeLa-GFP-LAMP1 bacterial artificial chromosome (BAC) cell lines were cultured in DMEM media complemented with 10% FBS, 1% penicillin-streptomycin and G418 (200 mg/L) at 37 °C and 5% CO_2.

For determining the uptake mechanism(s), we first transfected HeLa Kyoto cells with siRNA directed against CLTC (four different siRNAs), LDL receptor (LDLR, three different siRNAs), LDL related receptor (LRP1, three different siRNAs), Scavenger receptor (SRB1, three different siRNAs), Caveolin1 (CAV1, four different siRNAs), Rac1 (four different siRNAs), CTBP1 (four different siRNAs), Rabankyrin-5 (Rabnk-5, four different siRNAs) from Invitrogen or against CDC42 (three different siRNAs) from Ambion following protocol described in supplementary METHODS. Then, 72 h after the transfection, the cells were exposed to LNP-siRNA-alexa647 complemented with ApoE (see above) for 6 h, fixed with 4% PFA and imaged with automated microscope (see below). In order to exclude possible alteration of LNP uptake due to transfection pretreatment, we used both untreated cells and MOCK cells as control.

GFP silencing. HeLa GFP cells, GFP-Hepatocytes, Rab5-GFP human primary fibroblasts and GFP-NIH3T3 were transfected with LNPs formulation or naked siRNA-gold. After 72 h, the cells were fixed with PFA 4% (pH 7.2 in phosphate buffer) for 20 min at room temperature. After washing, cells nuclei were labeled with DAPI. Acquisition and analysis of images (at least 25 fields per condition) were done on an ArrayscanVTI with TwisterII automated widefield microscope (TDS, MPI-CBG, Dresden).

To relate LNP uptake to GFP silencing, we analyzed GFP downregulation after LNP uptake for different time points (1, 2, 3, 4, 5 and 6 h) followed by 72 h. GFP silencing was determined as above.

Immunofluorescence and uptake assay. For *in vitro* immunofluorescence analysis, cells were fixed in 4% paraformaldehyde at room temperature for 30 min, followed by two washes with PBS for 10 min. Subsequently, cells were incubated for 30 min in permeabilization solution (PBS; 0.5% Saponin), blocked in saturation solution (PBS; 3% BSA; 0.5% Saponin). Cells were then incubated 2 h at room temperature with primary antibodies in saturation solution, intensively washed 5 times for 5 min with the saturation solution. Finally, secondary antibodies, complemented with DAPI and Sytoblue (staining of nuclei and cytoplasm), were applied for 1 h at room temperature. After intensive washing, cells were kept in storage solution (PBS; 0.02% sodium azide). Images (at least 20 fields per conditions) were acquired on an Opera automated confocal microscope (TDS, MPI-CBG, Dresden) and analyzed using the MotionTracking software.

For *in vivo* immunofluorescence analysis, 4% PFA-perfused mice livers were embedded in OCT and 7-µm cryostats sections were cut. Sections were collected on super frost–treated glass slides and incubated at room temperature 5 min with glycine (0.1%) for aldehyde quenching, 10 min in PBS Tween20 (0.1%) for permeabilization, 2 h and 1 h, respectively, with first and secondary antibodies in saturation solution (PBS; 3% BSA). Then, sections were mounted with Mowiol and coverslip designed for high-resolution observation. Images (at least 15 fields per condition) were acquired on an Olympus Fluoview 1000 laser scanning confocal microscope (light microscopy facility, MPI-CBG, Dresden) equipped with an Olympus UPlanSApo 60× 1.35 oil immersion objective at a resolution of ~100 µm/pixel. Images were analyzed on MotionTracking.

Electron microscopy. Morphological experiments were analyzed in a blind fashion using a code that was not broken until the quantification was completed.

For EM analysis on HeLa cells, cells were transfected with LNP-siRNA-gold or free siRNA-gold and fixed with 2.5% glutaraldehyde (in phosphate buffer) overnight. Then, cells were post-fixed in ferrocyanide-reduced osmium. Cells were dehydrated in increasing bath of ethanol for 10 min, infiltrates with mixture of ethanol and Epon (3:1 and 1:3) and pure Epon for 1 h. After Epon polymerization overnight at 60 °C, the 24-well plates were broken and pieces of Epon were glued on Epon sticks. 70- to 50-nm sections were then cut and stained with uranyl acetate and lead citrate following classical procedure. Super-montaging of 100 images were randomly collected at 11,000× magnification on a Tecnai 12 TEM microscope (FEI) (electron microscopy facility, mpi-cbg, Dresden) and the images stitching was achieved using the open access software Blendmont (Boulder Laboratory, University of Colorado, USA).

For EM analysis of mice tissue, after injection of the formulation in the tail vein, mice were euthanized and livers were collected. Systematic uniform random sampling was obtained from different areas of the liver (**Supplementary Methods**). For each liver, five samples were collected and processed as previously described[11] (**Supplementary Methods**). Five montaging of 100 images per sample were randomly collected at 11,000× magnification on a Tecnai 12 TEM microscope (FEI) (electron microscopy facility, mpi-cbg, Dresden) and the images stitching was achieved using the open access software Blendmont (Boulder Laboratory, University of Colorado, USA).

Identification of organelles was based on morphological recognition as done previously[11] and is described in **Supplementary Methods**. Early endocytic compartment, late endocytic compartment, lysosome and mitochondria (used as control) containing gold were quantified in each montage. Because LNPs and intraluminal vesicles have a similar size and early endosomes and macropinosome are indistinguishable based on morphology, we did not discriminate between these compartments. Moreover, to quantify the total uptake, the ratio of structures labeled versus those unlabeled in a reliable manner and the number of gold found per μm^3, we applied a stereological approach (**Supplementary Methods**).

To quantify the ratio of siRNA escape from endosome, we developed a plug-in that automatically counts the total number of gold per montage. Images were processed to identify each gold particles (**Supplementary Methods**). Then, for a set of images, the particles were automatically counted and manually counted and we determined an error rate (<1%) confirming that our procedure succeeded in correctly identifying gold particles. Finally, we apply our procedure to determine the total number of gold particles in the images. Then, we manually count the number of gold particles within the cytoplasm based on morphological recognition.

Quantitative multiparametric image analysis. Quantitative multiparametric image analysis (QMPIA) was done in two sequential rounds of calculations. In the first round, aiming at the identification of fluorescent vesicles, the image intensity was fitted by a sum of powered Lorenzian functions[33]. The coefficients of those functions were then used to describe the features of individual objects (e.g., intracellular position relative to the nucleus, size, intensity, total

vesicular intensity). Additionally, nuclei and cells were identified by a pipeline involving several operations from morphological image analysis. Briefly, nuclei were found by a maximum entropy–based local thresholding and cells by a region-growing algorithm based on the watershed transform. In the second round, a set of statistics was extracted from the distributions of the endosome parameters measured in the first round. Statistical filters based on the mean intensity of the fitted object were then applied to remove the background and the unspecific staining (using control image with secondary antibody alone). This set of values, that quantitatively describes the fluorescence information of every channel in the image, has been used for comparing the different conditions as previously described[11].

Co-localization analysis was done by assessing the percentage of overlapping objects. Object "A" in channel "1" is considered to co-localize to object "B" in channel "2" if the integral intensity profile of A overlaps to the one of B more than a user-defined percentage threshold, here set to 40%. Co-localization was calculated both by number (percentage of LNP vesicles that are positive for LAMP) and by intensity volume (percentage of LNP in the LAMP-positive compartment). The described approach is more powerful than classical correlation and pixel co-occurrence analyses, because it allows us to (i) discriminate between background and foreground (object) fluorescence and (ii) interpret the results in terms of percentage of structures that are localized to objects in another channel of interest.

Western blot analysis. HeLa Kyoto cells seeded in 24-well plates, transfected for 0, 2, 4 and 6 h with unlabeled siRNA formulated LNPs, were lysates in 100 µl of lysis buffer (Meso scale Discovery lysis buffer containing CLAAP (1:1,000)). Protein concentrations were determined using DC Protein Assay (Bio-Rad Laboratories). Then, 20 and 12.5 µg of total proteins were run on SDS–polyacrylamide gel electrophoresis gels and blotted onto nitrocellulose membranes (XCell, Invitrogen). After antibody incubation the protein bands were detected using the Enhanced ChemiLuminescence solution reaction. ImageJ was used for quantification of blot intensities by measuring individual band intensities as described in the method outlined at http://lukemiller.org/index.php/2010/11/analyzing-gels-and-western-blots-with-image-j/. Briefly, for each band the intensity distribution was plotted. The basal background calculated from the mean of several areas surrounding the band was subtracted from the distribution and the area of the peak was calculated. The percent of surface area represented by each peak of one experiment was generated. The ratio of the sample percent versus the loading control percent was calculated to obtain a relative intensity. Finally, the relative intensity was normalized to the control set at 1.

Time-lapse fluorescence microscopy. HeLa GFP cells and BAC cell line HeLa-GFP-Rab5 and HeLa-GFP-LAMP1 were seeded on Ibidi cell-treated 'µ-slide 8-well' chambered coverslips and transfected with 20 nM alexa-647-siRNA formulated LNPs for 1.5, 2 and 4 h. Then, time-lapse fluorescent microscopy was acquired on a spinning disc fluorescent microscope (light microscopy facility, MPI-CBG, Dresden). For each time points 3 z-stacks (0.8-µm interval) were acquired every 5 s. Images were analyzed with MotionTracking after z-projection of the 3 z-stacks and identification of individual endosome by using single-particle tracking.

Statistical analysis. Data were expressed as the mean ± s.e.m. Statistical analysis was determined using unequal sample sizes and equal variance Student *t*-test. The two-tailed *P* values were added within the figure or the figure legends.

48. Damha, M.J. & Ogilvie, K.K. Oligoribonucleotide synthesis. The silyl-phosphoramidite method. *Methods Mol. Biol.* **20**, 81–114 (1993).
49. Soutschek, J. *et al.* Therapeutic silencing of an endogenous gene by systemic administration of modified siRNAs. *Nature* **432**, 173–178 (2004).
50. Addepalli, H. *et al.* Modulation of thermal stability can enhance the potency of siRNA. *Nucleic Acids Res.* **38**, 7320–7331 (2010).
51. Manoharan, M., Kesavan, V. & Rajeev, K.G. Modified iRNA agents. US Patent 7,745,608 (2010).

doi:10.1038/nbt.2612